

Electrically Reconfigurable Extended Lasing State in an Organic Liquid-Crystal Microcavity

Dmitriy Dovzhenko^{1*}, Luciano Siliano Ricco², Krzysztof Sawicki¹,
Marcin Muszyński³, Pavel Kokhanchik⁴, Piotr Kapuściński³,
Przemysław Morawiak⁵, Wiktor Piecek⁵, Piotr Nyga⁶,
Przemysław Kula⁵, Dmitry Solnyshkov^{4,8}, Guillaume Malpuech⁴,
Helgi Sigurðsson^{2,3}, Jacek Szczytko³, Simone De Liberato^{1,9}

¹School of Physics and Astronomy, University of Southampton,
University Road, Southampton, SO17 1BJ, United Kingdom.

²Science Institute, University of Iceland, Dunhagi-3, Reykjavik, IS-107,
Iceland.

³Institute of Experimental Physics, Faculty of Physics, University of
Warsaw, ulica Pasteura 5, Warsaw, PL-02-093, Poland.

⁴Institut Pascal, Université Clermont Auvergne, CNRS, ClermontINP,
Clermont-Ferrand, F-63000, France.

⁵Institute of Applied Physics, Military University of Technology, S.
Kaliskiego 2, Warsaw, 00-908, Poland.

⁶Institute of Optoelectronics, Military University of Technology, S.
Kaliskiego 2, Warsaw, 00-908, Poland.

⁷Institute of Chemistry, Military University of Technology, S. Kaliskiego
2, Warsaw, 00-908, Poland.

⁸Institut Universitaire de France, Paris, F-75231, France.

⁹Istituto di Fotonica e Nanotecnologie, Consiglio Nazionale delle
Ricerche (CNR), Piazza Leonardo da Vinci 32, Milano, 20133, Italy.

*Corresponding author(s). E-mail(s): dovzhenkods@gmail.com;

Abstract

Small-footprint, low-power arrays of coupled coherent emitters with the capability of near- and far-field engineering and coherence control are highly sought after to meet modern nanophotonics evolving needs. Between existing solutions based

on vertical-cavity surface-emitting lasers, phase masks in bulk traditional cavity-based systems, and lattices of exciton-polariton condensates, only the strongly light-matter coupled systems were shown to be capable of controlled on-chip interaction between the individual coherent states while often operating at cryogenic temperatures. Here we demonstrate electrically controlled in-plane interaction between optically reconfigurable spatially separated lasing states, operating at room temperature in the weak light-matter coupling regime. We show spatially extended coherent lasing state or "supermode" with wide-range micro-scale control of near-field, far-field and on-chip phase-locking tuning functionality. An extended lasing state appears due to near-field transverse coupling between distinct spatially pumped lasing states in the plane of an organic liquid crystal-filled microcavity. We realize electrical control over the interaction strength between lasing states and corresponding mutual coherence going beyond nearest neighbours through electrical tuning of the microcavity optical modes with external voltage, and a spin-selective directional coupling regime by using a photonic analogue of the Rashba-Dresselhaus spin-orbit interaction.

Keywords: liquid crystal microcavity, Rashba–Dresselhaus spin-orbit coupling, electrical tuning, phase-locking, dyad coupling, lasing, optical lattice

1 Introduction

Creating compact and reprogrammable sources of coherent emission is a central task for developing modern integrated photonic devices. Of separate interest is the realisation of phase-locking in arrays of coherently emitting lasers for beam shaping [1], topological optics [2], investigation of many-body phenomena with optical simulations [3, 4] and in the emerging fields of all-optical neural networks [5, 6] and reservoir computing [7, 8], where optical networks are beneficial due to the high clock rates, parallelism and low losses.

Several approaches have been developed to achieve the phase-locked arrays of lasers, including shaping bulk laser beams with diffractive elements, free-form optics, metasurface arrays, or spatial light modulators [2, 9, 10], and phase-locking of the vertical-cavity surface-emitting laser (VCSEL) arrays [11, 12]. Despite recent technological advances existing solutions usually require either external devices to provide optical feedback and phase injection locking or utilise irreversible fabrication techniques such as beam shaping using metasurface-integrated VCSELs [13] and photonic crystal surface-emitting lasers [14–16].

An alternative approach to compact on-chip optical devices with good in-situ tunability over the emission characteristics is realised with optical lattices of non-equilibrium exciton-polariton Bose-Einstein condensates [17, 18] which, due to their strong nonlinearities and optically tunable ballistic coupling mechanism [19], are being explored as promising reconfigurable elements for all-optical computing [20, 21], spin simulation [4, 22], angular momentum generation [23, 24], topologically protected lasing [25–27], and more. Although many of the aforementioned works have been conducted at cryogenic temperatures in II-VI or III-V semiconductor quantum well

microcavities, increasing effort has been shifted towards more application-friendly room temperature materials [28–30], in particular organic materials relevant to the current study [31–33]. However, for room temperature organic-based light-emission devices, the coherent emission usually appears perpendicular to the cavity surface (at $k_{\parallel} = 0$) and therefore coupling between the emission nodes (i.e., pumped condensates) is hard to achieve and usually requires significant overlap between the condensate wave-functions [31, 32, 34]. Besides, the requirement for strong light-matter coupling imposes strict conditions on the parameters of both photonic and excitonic components of the system, restricting tuneability and scalability. In this work we attempt to fill the gap between the optically reconfigurable ballistic lattices of polaritonic condensates and tuneable organic microcavities operating at room temperature in the weak light-matter coupling regime, where in-plane phase-locking between separated optically excited lasing states has yet not been reported.

Here we present a realisation of spatially extended lasing supermodes formed by coherent in-plane coupling between individually pumped lasing states with all-optical control over the geometry of phase-locked lasing domains at room temperature in the weak light-matter coupling regime. We demonstrate electrical control over mutual coupling between the lasing states allowing for a wide-range shaping of the near- and far-field of the arrays of coherently coupled emitters, see Fig. 1(a) for schematic. We utilize a liquid crystal (LC) dye-filled microcavity (LCMC) in the weak light-matter coupling regime, with the photonic wavefunction of the supermode directly accessible by measuring the emission intensity in real space. From here on, a single “lasing state” refers to a spatially localized emission site (node) in the microcavity plane that is being optically pumped above threshold with a corresponding tightly focused, normal incidence, nonresonant Gaussian beam. By optically reconfiguring the profile of the incident nonresonant excitation beam into multiple spots, one can easily control the pumping geometry and arbitrary shape of the resulting extended lasing state. The ballistic near field coupling, and subsequent synchronization, between individual lasing states in the plane of the cavity is defined by their in-plane photon momentum component which determines their mutual overlap between the pumped gain regions. Amazingly, the coupling can be controlled electrically by applying a voltage to the LC-filled microcavity, see Fig. 1(a,b), which rotates the birefringent molecules, changing the dielectric cavity tensor, and subsequently the in-plane dispersion relation of the cavity photons. At higher voltages, where the transverse electric (TE) mode is tuned into resonance with the next order transverse magnetic (TM) mode of opposite parity [35] an effective Rashba-Dresselhaus (RD) spin-orbit coupling (SOC) of the photon dispersion emerges, providing a way to realise spin-selective directional coupling of lasing states [36]. We further investigate the polarization inheritance properties of the system and realize the unconventional coupling regime between lasing states extending beyond the nearest-neighbour approximation. Based on the demonstrated properties of our system new class of photonic systems can be developed with unexpected functionality of all-optical reconfigurable geometry, in-plane coherence control and electrical tuneability at room temperature, paving the way towards all-optical computing and lattice physics on chip in the weak light-matter coupling regime.

2 Results

2.1 Platform design and approach

Our lasing device is an electrically tunable planar microcavity operating in the weak light-matter coupling regime containing a LC solution with homogeneously dispersed pyrromethene 580 (P580) laser dye, Fig. 1(a) [see Methods for more details on the sample and experimental procedure]. By applying external voltage that changes the spatial orientation the birefringent LC molecular director, we can electrically tune the splitting between the transverse electric (TE) and transverse magnetic (TM) cavity modes which can enable intriguing photonic analogues of SOC such as the optical spin-Hall effect [37, 38] and RD SOC [39–41]. We define the plane of cavity as the x - y plane and the corresponding momentum plane with k_x - k_y coordinates. We also define vertical polarization (V) as linear polarization along y , and horizontal polarization (H) along x . Under applied voltage the LC molecules tilt in the y - z plane where z is the out-of-plane direction, or direction of emission.

Fig. 1(c,d,e) shows energy-resolved momentum space photoluminescence (PL) of the lasing state below and above the lasing threshold at different voltages, nonresonantly pumped with a single vertically polarized Gaussian spot. Below the threshold (left half of panels) both horizontally and vertically polarised dispersion curves are visible. When external voltage is applied, we observe a shift of the vertically polarised subset of cavity Fabry-Pérot modes towards higher energy due to the increase of the refractive index coming from the LC reorientation inside the cavity for vertically polarised light, while horizontally polarised modes remain unchanged [compare Fig. 1(c) with 1(d)]. When two orthogonally linear polarised modes of opposite parity (i.e. different longitudinal mode index) are brought in resonance by electrical tuning, the system enters the RD SOC regime [35, 41], shown in Fig. 1(e). The dispersion valleys then become circularly polarised with opposite circular polarisations symmetrically shifted in Fourier space along the k_x axis. At sufficiently low momenta, the in-plane dispersion relation for σ^\pm circularly polarized photons can be written

$$E_\pm = \frac{\hbar^2 k_\parallel^2}{2m} \pm \delta_{\text{RD}} k_x \quad (1)$$

where m is the effective photon mass and $\delta_{\text{RD}} > 0$ defines the valley separation $2\delta_{\text{RD}}m/\hbar^2$. Above the lasing threshold, we observe the collapse of the emission to a narrow energy state laying slightly above the bottom of the cavity photon dispersion curve. The linear polarization of the emission corresponds to the linear polarisation of the pump as seen in the normalized momentum space S_1 Stokes parameters of the emission in Fig. 1(f) for the 0 mV and 1600 mV cases [see Eq. (3) for definition of the Stokes parameters and connection to the emission polarization]. In the RD SOC regime at 1840 mV, both circular components are present simultaneously in their respective valleys as seen in the S_3 Stokes parameter [see Eq. (3) and Fig. 1(f)]. Further details on polarisation inheritance are presented in Sec. 1.1 of Supplementary Information (SI).

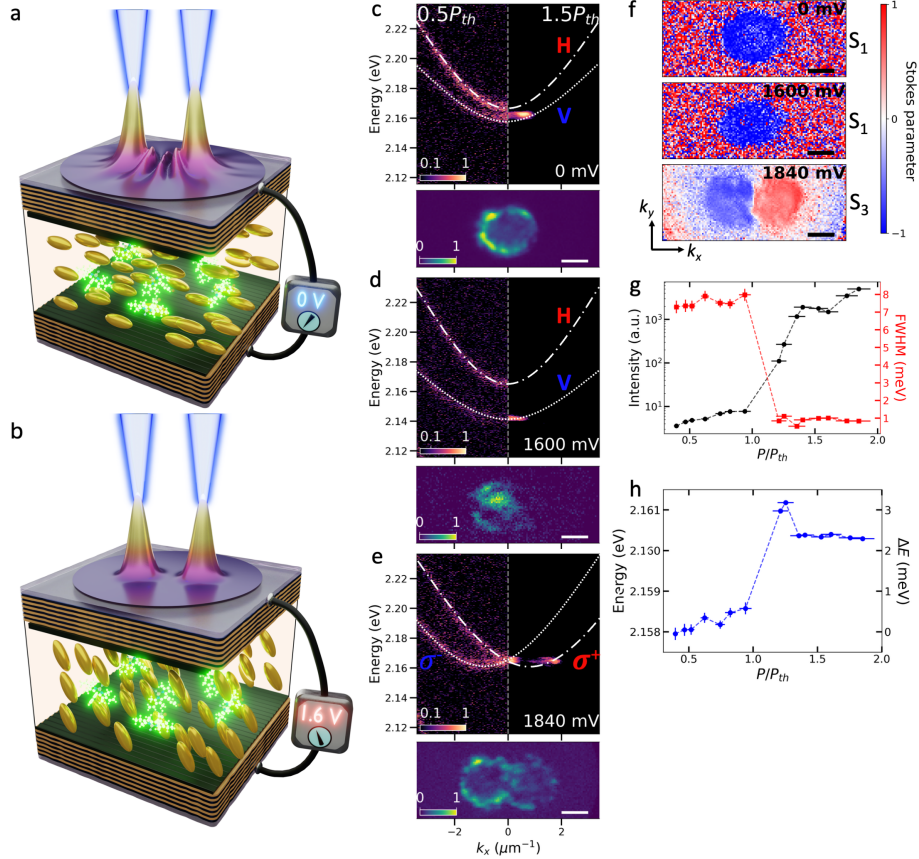


Fig. 1 Electrically controlled dyad lasing supermode and the blueshift-induced in-plane momentum of coherent emission from a single lasing state. (a,b) Schematic showing the microcavity filled with liquid crystals and P580 laser dye pumped in a dyad configuration with (a) phase-locked spatially extended supermode without external voltage applied and (b) two uncoupled lasing states at 1600 mV voltage correspondingly. Emission characteristics of a single lasing state: (c-e) (above) energy-resolved momentum-space along $k_y = 0$ for three values of external voltage, corresponding to (c) 0 mV, (d) 1600 mV, and (e) 1840 mV, pumped below ($0.5P_{th}$, left) and above ($1.5P_{th}$, right) the lasing threshold for each case and (below) momentum-space pumped above ($1.5P_{th}$) the lasing threshold, dot-dashed and dotted curves show (c-d) horizontally and vertically polarised or (e) right-circularly and left-circularly polarised cavity modes; (f) momentum-space distribution of the normalised S_1 (top and middle) and S_3 (bottom) Stokes components corresponding to momentum-space at (c-e); (g) photoluminescence intensity (black circles), full-width at half-maximum (FWHM, red squares), and (h) energy of the lasing state versus pump power at zero voltage, extracted from the fitting of the emission spectral profile obtained by integrating dispersion data around $k_x = 0$ over $\pm 0.2\mu\text{m}^{-1}$ of the energy-resolved momentum space measurements. For better visibility energy resolved images (c-e) are illustrated in logarithmic scale saturated below 0.05.

Figure 1(g,h) presents the dependence of PL intensity, FWHM, and emission energy on the pumping power at 0 mV external voltage. Initially, a linear increase in intensity is observed, followed by a sharp nonlinear behaviour accompanied by a step-like

drop in FWHM, both hallmarks of a transition from spontaneous emission to photonic lasing. This transition is further evidenced by a sharp blueshift of the emission relative to the cavity dispersion minimum below threshold. In conventional inorganic systems, such as GaAs-quantum well microcavities with Wannier–Mott excitons, such blueshift near threshold is a recognized signature of polariton lasing [42]. However, this interpretation does not straightforwardly apply to organic microcavities with Frenkel excitons, which are highly localized and do not support comparable repulsive interactions. It has been shown [43, 44] that, in organic systems, the blueshift primarily arises from the saturation of molecular transitions and the associated refractive index change and hence, is present in both weak and strong light-matter coupling regimes and, importantly, is wavelength dependent, see Fig 1(c,d,e). Under tight optical pumping, it creates a localized potential sufficient to induce the outflow of coherent photons with finite average absolute value of in-plane momentum ($k_{\parallel} \neq 0$), resulting in ring-shaped emission in momentum-space (or two split rings relative to $k_x = 0$ in the RD regime), with the radius k_l determined by the amount of pump-induced blueshift [see momentum-space PL at the bottom of Figs. 1(c,d,e)]. This ring is similar to resonant Rayleigh scattering ring when waves are scattering of disorder and couple to many different momenta [45]. Moreover, for tuneable LCMCs, this blueshift depends on the spectral detuning between the P580 dye absorption and the cavity mode, which can be modulated via applied voltage [Fig. 1(c,d)]. Consequently, the k -space profile of the coherent emission is electrically controllable through the modulation of the local potential. While the underlying mechanisms differ between room-temperature organic microcavities and cryogenically operated GaAs-based systems, both generate coherent emission with finite in-plane momentum, which is a key requirement for mutual phase-locking between lasing sites and the emergence of spatially extended lasing "supermodes" via in-plane coherent energy exchange.

2.2 Dyad lasing supermode

To demonstrate the realisation of coupled extended lasing supermodes formed by phase-locking of two spatially separated lasing modes, we excite the microcavity with vertically polarised two-spot pump profile (i.e., a lasing dyad) with interspot separation distance d in the range of 9 to 19 μm , see Fig. 2. We keep the microcavity at 0 mV external voltage corresponding to the cavity regime shown in Fig. 1(c), where single lasing state occurs with the blueshift $\Delta E \approx 3.0$ meV and corresponding in-plane momentum $|k_l| \approx 1.0 \mu\text{m}^{-1}$ relative to the bottom of the vertical dispersion band $E_0 \approx 2.16$ eV. RD SOC is not observed as horizontally and vertically polarised cavity modes are slightly separated in energy.

Fig. 2(a-f) shows the experimentally measured real- (a-c) and momentum- (d-f) space distributions of the PL from the spatially extended supermode lasing state formed due to the mutual exchange of coherent photons out-flowing from each of the two individually pumped lasing spots. In the absence of coherent energy exchange one would observe two independent lasing spots in the real space with the PL intensity monotonically decaying outside of the pumping spot areas, Fig. 1(b), while Fourier-space would have a ring-shaped pattern similar to the single state case. Instead, here we observe phase-locking between two individually pumped lasing states, evidenced

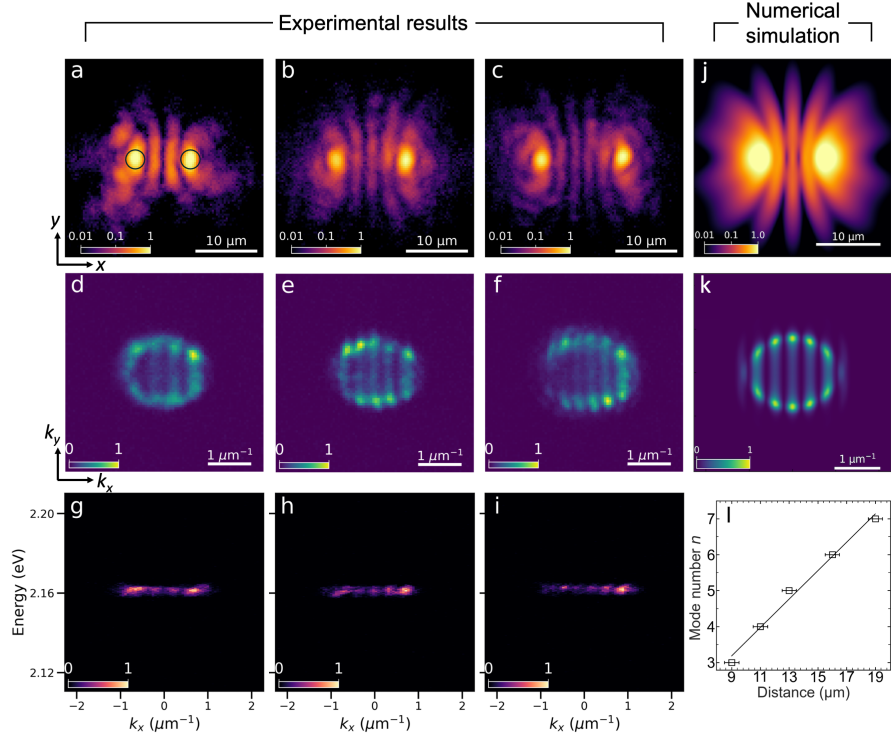


Fig. 2 Dyad supermode lasing state. (a-i) Experimental images of the dyad supermode lasing state emission in (a-c) real-space, (d-f) momentum space, and energy-resolved momentum-space along $k_y = 0$ (g,h,i) for two pump spots (black circles) separated by (a,d,g) 9 μm , (b,e,h) 11 μm , and (c,f,i) 13 μm . (j,k) Numerically simulated (j) real-space and (k) momentum-space distribution of the supermode lasing state emission corresponding to the experimental data at (b,e). (l) Dependence of the extended lasing state mode number n on the pump separation distance. Each spot was pumped with the fixed spot size Gaussian beam at $P_{1,2} = 1.5P_{th}^{(1)}$, where $P_{th}^{(1)}$ is the lasing threshold for a single isolated lasing state. For better visibility real-space images (a-c,j) are illustrated in logarithmic scale saturated below 0.01.

by a characteristic oscillatory interference pattern of PL intensity in both real and Fourier spaces along the axis connecting the pump spots. This interference pattern directly reveals a macroscopic coherent wavefunction extending over distances up to $d = 20\mu\text{m}$. The resulting dyad lasing supermodes exhibit either even or odd parity with respect to their reflection axis at $x = 0$. The parity is determined by the relative

phase between the lasing centres ($\Delta\phi = 0$ or π), depending on the separation d between the pump spots, as expected and observed previously for polariton dyads [46]. Maximum intensity at the midpoint indicates in-phase synchronisation ($\Delta\phi = 0$), while a minimum of the intensity in the centre reflects anti-phase synchronisation ($\Delta\phi = \pi$). In both cases, a single mode of corresponding parity was present in energy-resolved Fourier-space PL [Fig. 2(g-i)]. We quantitatively characterise the supermode by introducing the mode number n corresponding to the number of nodes between the pump spots analogous to the mode numbers used to describe the higher-order Hermite-Gaussian transverse modes. A linear increase in the mode number n of the spatially extended supermode is visible when the distance between pumping spots d is increased, Fig. 2(l).

To theoretically reproduce the real and Fourier-space PL from the dyad lasing state, we perform numerical simulations based on a two-dimensional (2D) non-Hermitian Schrödinger equation under drive and dissipation (a simplified version of Maxwell-Bloch equations [47, 48]). Details about the theoretical model employed are presented in Methods (Sec. 4.3). In Fig. 2(j,k) we show the simulation results for the dyad lasing state separated by $d = 11 \mu\text{m}$ corresponding to the experimental data presented in Fig. 2(b,e). Corresponding simulations of the lasing states for $d = 9 \mu\text{m}$ and $13 \mu\text{m}$ can be found in the SI. The slight mismatch between the experimental and numerically obtained data is due to the local disorder morphology of the sample and is mostly present in real-space PL profiles.

In order to highlight the isotropy of the coupling at 0 V we demonstrate in Fig. 3 the phase-locking in a square 2×2 lattice pump geometry (shown here rotated by 45° in cavity plane) with anti-phase synchronisation between nearest neighbours ($\Delta\phi_{i,i+1} = \pi$).

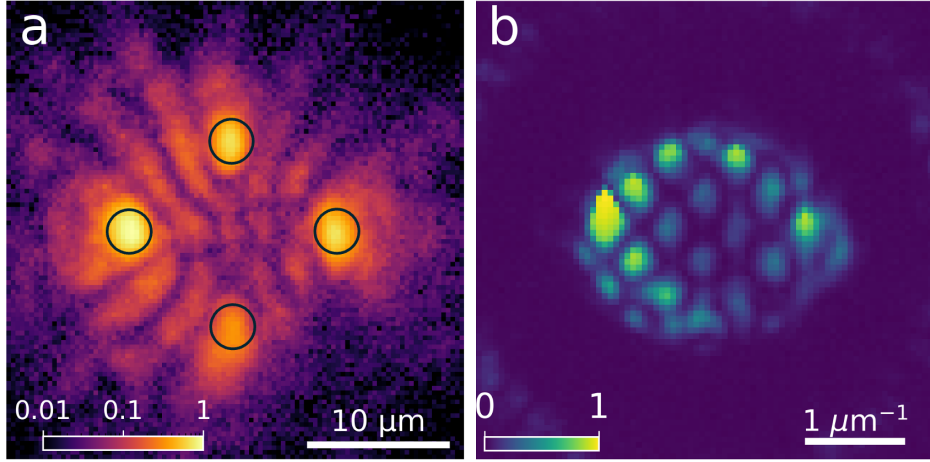


Fig. 3 Two-dimensional lattice supermode. (a-i) Experimental images of the supermode lasing state emission in (a) real-space, (b) momentum space for the 2×2 lattice pump geometry (black circles).

The phase-locking between the spatially separated lasing states is further supported by the spatial coherence measurements, see in Supplementary Information Sec 1.2 for details. We therefore refer to these phase-locked lasing states as a lasing supermode or a dyad supermode in the particular case of two phase-locked states. Such a phase-locking mechanism implies that the resulting mode parity depends not only on the spatial separation but also on the in-plane momentum (k_l) of the coherent emission. While we have demonstrated the dependence of the supermode parity on distance for a fixed k_l , the latter can be tuned electrically in our system, as discussed in Sec. 2.1.

2.3 Electrical control over coupling in a dyad lasing supermode. Coupling in the presence of spin-orbit interaction.

Electrical control of the cavity photon dispersion is one of the major advantages of the LCMCs. As we have shown in Sec.1, the blueshift above the lasing threshold is wavelength dependent and at the specific regimes of cavity detuning it provides a way to alter the value of in-plane momentum (k_l) of the lasing state emission. Below we demonstrate that the efficiency of coupling in a dyad lasing supermode is defined by this in-plane momentum distribution. Hence, electrical tuneability of the cavity opens a way to reversibly control the coupling between the spatially separated coherent lasing states and to shape the emission of lasing supermode in momentum space.

In Fig. 4 we show the experimentally measured real- (a-d) and momentum-space (e-h) distributions of the dyad PL corresponding to four distinctive regimes of coupling between the two pumped lasing spots, controlled by an applied external voltage V ranging from 0 to 1880 mV. The first regime of interaction is shown in Fig. 4(a,e) and corresponds to the case of minor energy detuning between horizontally and vertically polarised modes at 0 mV external voltage with the bottom of the vertical dispersion band $E_0 \approx 2.16$ eV [Fig. 1(c)]. Similar to the dyad supermode described in Sec. 2.2, one can observe a bright interference fringe at the mirror symmetry axis ($x = 0$ and $k_x = 0$) indicating spontaneous phase locking of the lasing nodes into a macroscopic even parity mode. In contrast, when voltage of 1600 mV is applied, see Fig. 4(b,f), the coupling between the lasing spots is severely reduced evidenced as lack of interference fringes in both real and Fourier space. In this scenario, the PL is mostly localized to the pump gain regions in real space with no apparent expanding envelope of outflowing photons, as seen from the corresponding Fourier space PL which displays a wide Gaussian distribution centered around $k_{||} = 0$ in sharp contrast to the ballistic ring. This is due to the significant negative energy detuning of the vertically polarised cavity mode relative to the zero voltage condition and the corresponding drop of the blueshift ($\Delta E < 0.3$ meV) when pump is also vertically polarised. Indeed, a lower pump-induced blueshift for the pumped photons in each lasing state means that the radially expanding part of the wavefunction acquires smaller kinetic energy and therefore slower outflow velocity away from the pump spot. This is seen as a decrease of the in-plane component of the emission k_l in momentum space as discussed in Fig. 1(d) for the single pump spot. As a result, the overlap between neighbouring lasing states decreases and their coupling diminishes with consequent lack of interference fringe contrast.

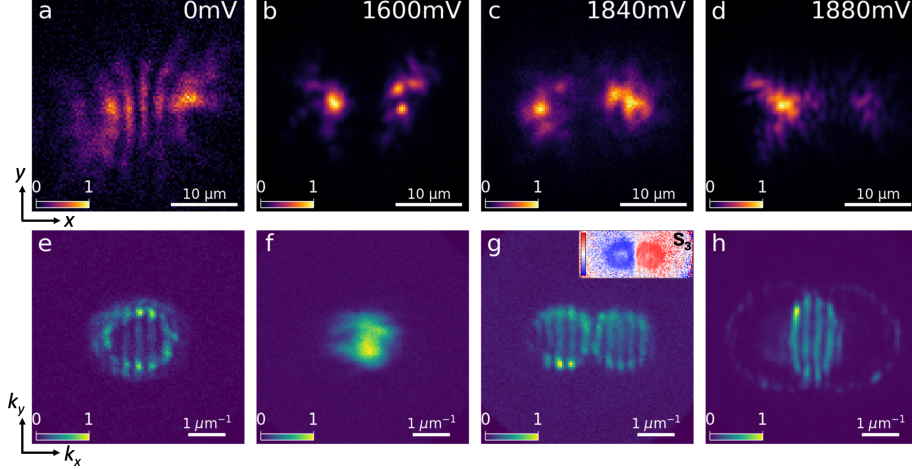


Fig. 4 Electrical control of coupling in a dyad supermode lasing state. Experimental images of the lasing state emission in (a-d) real-space, (e-h) momentum space for two pump spots at (a,e) 0 mV, (b,f) 1600 mV, (c,g) 1840 mV and (d,h) 1880 mV, showing (a) coupled supermode lasing state, (b) uncoupled separate lasing spots, and (c) and (d) extended lasing state in RD regime and slightly detuned from RD regime, respectively. Inset in (g) shows the corresponding momentum-space distribution of the $S_3(\mathbf{r})$ normalised Stokes component of the emission. Each spot was pumped with the fixed spot size Gaussian beam, separated by the fixed distance of $13 \mu\text{m}$ at $P_{1,2} = 1.5P_{th}^{(1)}$, where $P_{th}^{(1)}$ is the lasing threshold for a single isolated lasing state.

Amazingly, in Fig. 4(c,g) we observe revival of the dyad coupling when entering the RD SOC regime at higher voltages $V = 1840 \text{ mV}$. Here, mixing between two distinct cavity modes results in a dispersion relation made of two off-centred cross-circularly polarized parabolas or valleys, displaced along k_x axis parallel to the axis of the dyad [see Eq. (1) and Fig.1(e)]. Since the bottom of each dispersion branch remains similar in energy to that of the vertically polarised cavity mode at $V = 0 \text{ mV}$, the wavelength-dependent PL blueshift above the threshold is unchanged compared to the initial case [Fig.1(c,e)], as is the corresponding ring radius in each valley in Fourier space [Fig.4(e)]. Here, we observe emission from two separate ballistic rings in Fourier space displaced symmetrically along k_x with opposite circular polarisation corresponding to iso-energy curves of each paraboloid (see the inset in Fig. 4(g) for $S_3(\mathbf{k}_{\parallel})$ Stokes parameter distribution in momentum space). We note that due to RD SOC this regime demonstrates spin-dependent anisotropy of the supermode emission with $\langle k_x^{\sigma+} \rangle > 0 > \langle k_x^{\sigma-} \rangle$ and $\langle k_y^{\sigma+} \rangle = \langle k_y^{\sigma-} \rangle = 0$ with a clear fringe pattern observed in Fourier space, proving the phase-locking revival between the two pumped lasing states. Phase-locking revival was also observed in restoring of spatial coherence in the interferometry measurements, see in SI. In real space the intensity of the fringes between the pump spots is lowered relative to the case of $V = 0 \text{ mV}$. We attribute this to the local inhomogeneity affecting the real space distribution due to the reorganisation of LCs under external voltage.

As the voltage is increased even further to 1880 mV [see Fig. 4(d,h)], the system is shifted out of the RD SOC regime with a subsequent gap opening at branch crossing point $k_{\parallel} = 0$ with linearly polarized states forming at low momenta. The new dispersion relation, sufficiently close to the RD SOC resonance, can be approximately written as,

$$E_{\pm} = \frac{\hbar^2}{2} \left(\frac{k_x^2}{m_x} + \frac{k_y^2}{m_y} \right) \pm \sqrt{(\delta_{\text{RD}} k_x)^2 + \delta^2} \quad (2)$$

where $m_{x,y}$ are renormalized effective photon masses along the x and y directions [35] and δ describes splitting between horizontal and vertical linear polarized modes at $k_{\parallel} = 0$. The modified dispersion leads to a higher photon population in the mode with linear polarisation component parallel to the pump polarization. The emission still partially occupies two ballistic circles in the momentum space PL as seen at high wavenumbers in Fig. 4(h). The radius of the circles is larger since the emission energy is now located further above the minimum of the dispersion (2). Interestingly, here the dyad mostly populates the low momentum intersect between the two circles in momentum space corresponding to photons with mostly linear vertical polarization projection. The result is a peculiar distribution of the emission in Fourier space in which the emission anisotropy is reversed relative to the case of pure RD SOC regime ($\langle |k_y| \rangle > \langle |k_x| \rangle$). Control of the in-plane momentum anisotropy is another important feature of our system as it potentially offers a way for the realisation of a direction-dependent coupling in two-dimensional arrays of phase-locked coherent emitters. Similar to the previous case the fringe pattern in real space is distorted and observable only around pumping spots. However, it is clearly visible in the Fourier space over the whole area of emission distribution. We verify our interpretation through 2D non-Hermitian Schrödinger (paraxial Maxwell-Bloch) simulations shown in Fig. 5, see Sec. 4.3 for details.

2.4 Unconventional coupling in 1D lasing supermode

In coherently coupled photonic systems the nearest-neighbour (NN) coupling dominates over the next-nearest-neighbour (NNN), including systems based on coupled lasers [49], VCSELs arrays, polaritonic and photonic lattices [3]. This is easily understandable, as the coupling strength is usually defined by the mutual overlap of the coupled states wavefunctions, which decay exponentially with the distance from each state centre. Overcoming this behaviour is of prior importance for universal applications of coherently coupled photonic arrays as all-optical simulators [50]. The possibility of NNN coupling with polaritonic condensates in GaAs-based microcavities at cryogenic temperatures has been shown previously using distance-dependant spin-screening of NN interaction leveraging the optical spin Hall effect [51]. Same approach based on the TE-TM field is not straightforwardly applicable in organic microcavities, but it can be adapted, because the polarisation basis in these systems is defined by horizontal and vertical components, following the orientation basis of the molecular dipole moment. As we show above, the polarisation of the lasing state is then inherited from the pump polarisation and is linear as long as SOC remains small, see Sec. 2.1. As a result, the efficient coupling between the lasing spots is only possible while they share the same linear polarisation inherited from the pumps. In Fig. 6 we

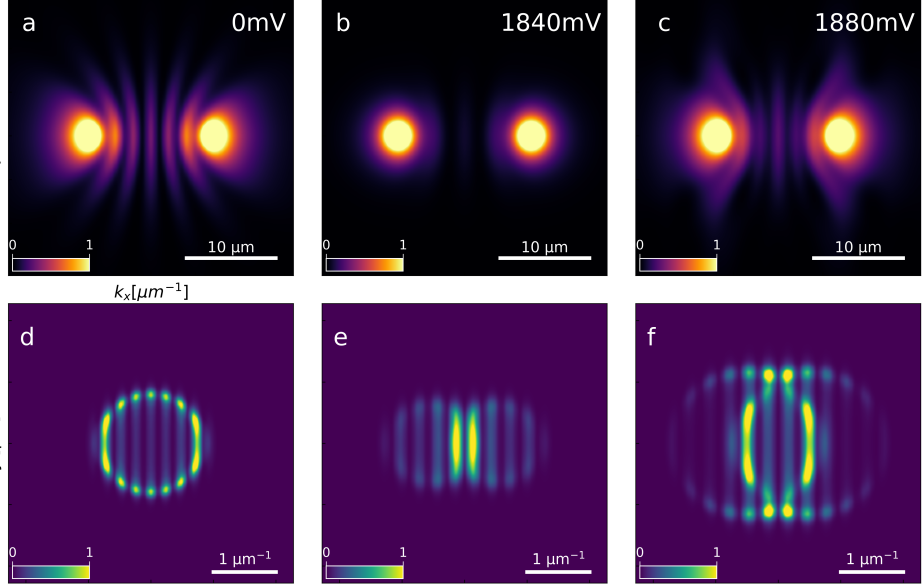


Fig. 5 Simulation for an electrically tuneable coupling in a dyad configuration corresponding to profiles shown in Fig. 4, for $V = 0$ mV (a,d), 1840 mV (b,e) and 1880mV (c,f), respectively.

demonstrate the realisation of NNN coupling regime in a chain of 3 coupled lasing states, by measuring the real space PL (a-c), momentum space PL (d-f), and (g-i) real space S_1 Stokes parameter of the non-normalized Stokes vector of the extended lasing state emission [see Eq. (3)]. The corresponding numerical simulations obtained via the 2D non-Hermitian Schrödinger model are shown in the Sec. 4.3.

First, we project the two spot excitation pattern similar to the one shown in Sec 2.2 with two horizontally polarised pumping spots separated by $d = 20 \mu\text{m}$ distance, see Fig. 6(a,d,g). The extended horizontally polarised lasing supermode of the odd parity ($\Delta\phi = \pi$ phase difference) is formed as evidenced in both real- and Fourier-space. We then project an additional horizontally polarised pumping spot in the middle between the initial two spots, making pump spots pairwise separated by $d/2 = 10 \mu\text{m}$, as shown in Fig. 6(b,e,h). The "triad" supermode coherent state is verified in both real and Fourier space with a π phase difference between each pair of the phase-locked lasing states. Interestingly, two subsets of fringes are distinguishable in the Fourier-space. One with the same period of the fringes as for a dyad but with a lower relative intensity, showing phase-locking between outer states and the second at a higher intensity and a period two times larger, showing strong phase-locking between each pair of the nearest neighbours.

However, when we flip the polarisation of the central pump spot to the vertical one, both real and Fourier-space distributions change dramatically, see Fig. 6(c,f,i). First, the fringes in the real space are not visible, due to the low intensity similar to the

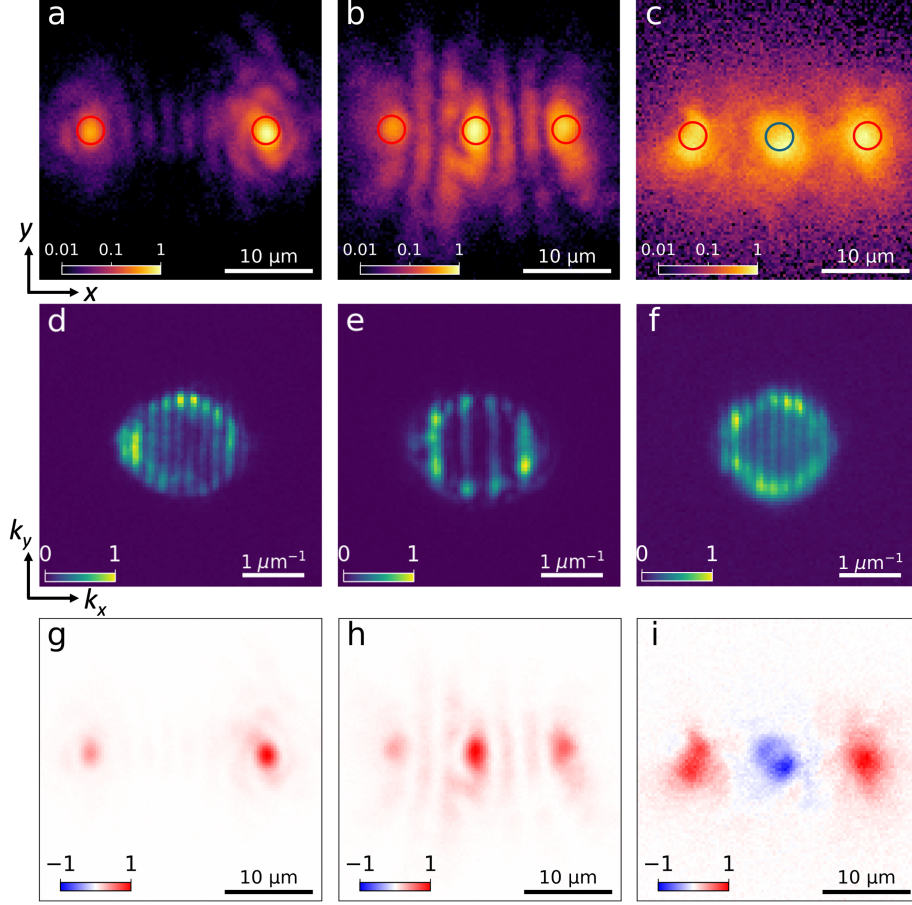


Fig. 6 Unconventional coupling in a 1D chain of pump spots. Experimentally measured (a-c) real-space, (d-f) momentum space, and (g-i) real-space S1 component of the Stokes vector of the lasing state emission. (a,d,g) Left panel shows data corresponding to the two pump spots at $20 \mu\text{m}$ separation distance with horizontally polarized pump (red circles), (b,e,h) central panel shows data for three horizontally polarized pump spots separated by $10 \mu\text{m}$, (c,f,i) right panel shows data for three pump spots separated by $10 \mu\text{m}$ with central spot pumped with vertically polarized light (blue circle). All measurements were done at zero external voltage. For better visibility real-space images (a-c) are illustrated in logarithmic scale saturated below 0.01.

case of the far-separated dyad [Fig. 6(a)]. The Fourier space shows a superposition of two states. The first originates from a NNN type of coupling between the edge states which is visible with the odd parity and the same periodicity as the one observed for the far-separated dyad. The second mode is ring-shaped and corresponds to the Fourier space profile of an isolated central lasing state. Thus we eliminate the coupling

between the nearest neighbours by exciting the lasing state in the middle with the opposite polarisation to the outer pump spots, while the NNN coupling is still present.

3 Discussion

In conclusion, we have demonstrated the emergence of spatially extended lasing supermode states in a LC dye-filled microcavity with all-optical control over coherent emission in both near- and far-field. We achieve the phase-locking between spatially separated independently pumped lasing states by realising mutual coherent photon exchange leveraging the excitation of high in-plane momentum lasing states at each pumping spot. By tuning the separation distance between the lasing states, we demonstrate phase-locking with either 0 or π phase difference extending over distances up to $d = 20\mu\text{m}$. Moreover, by applying an external voltage and achieving effective wave retardation in an anisotropic LCMC, we have introduced electrical control over coupling strength between individually pumped lasing states. Thus we alter the intrinsic properties of the supermode extended lasing state by shaping its near- and far-field distributions.

We have also shown the switching on and off mechanism of coupling into spatially extended lasing supermode in a reversible manner, along with the ability to bring anisotropy in the Fourier space distribution of the PL in both k_x and k_y directions. Moreover, in the RD SOC regime, the emission from the supermode lasing state becomes circularly polarised, the coupling becomes spin-selective and the supermode emission with opposite spin separates in Fourier space. These findings open prospects to create fully optical systems with spin propagation control employing external voltage and optical excitation profile engineering. Utilising the inheritance of the pump polarisation by the supermode coherent emission, we experimentally demonstrate a non-trivial regime of coupling in a chain of phase-locked extended lasing states. In particular, we show that next-nearest-neighbour coupling can be tuned stronger than the nearest-neighbour coupling, which is an important limitation in the majority of experimental platforms for the investigation of many-body phenomena. We have focused here on the properties of one-dimensional supermode, but in the future, two-dimensional lattices of coupled lasing states can be developed with the prospect of exploring non-Hermitian physics, topologically protected states [52, 53], and as a solid platform for photonic simulator [3, 22, 54] and all-optical neural networks [5, 6, 55] operating in a weakly coupled regime at room temperature.

4 Methods

4.1 Fabrication of the dye-filled microcavity with LC molecules

The microcavity consists of two Distributed Bragg Reflectors (DBRs) with the solution of highly birefringent nematic liquid crystal and P580 dye molecules sealed in the cavity region between them. Each DBR is composed of six pairs of $\text{SiO}_2/\text{TiO}_2$ layers, centered at $\lambda = 560\text{ nm}$ (2.21 eV), and deposited on a 26 nm transparent ITO electrode on a glass substrate to allow for electrical control over the orientation of LC molecular director by applying an external voltage, see schematic of the device in Fig. 1(a).

The DBRs are assembled using adhesive containing silica spacers, ensuring a cavity thickness varying wedge-like between 2.5 μm and 3 μm . Antiparallel orienting layers (SE-130, Nissan Chem., Japan) were applied to both substrates via spin-coating. The cavity was then filled by capillary action with a high-birefringence, home-made liquid crystal mixture, LC2091* (refractive indices: $n_o = 1.57$, $n_e = 1.98$ at 589 nm, sodium D-line) in the nematic phase, with pyrromethene 580 (P580) laser dye (1% by wt.) dispersed in the mixture. The elongated shape of the LC molecules provides refractive index anisotropy in x - y plane of the cavity ($\Delta n(V = 0) = n_e - n_o = 0.41$), while external voltage applied to the ITO contact rotate the LC director in y - z plane of the cavity [56, 57]. Consequently, control over the energy of the vertical linearly polarised set of optical cavity modes parallel to the y -axis is achieved [37]. The set of horizontal linearly polarised modes parallel to the x -axis remains unchanged [Fig. 1(b,c)].

4.2 Optical spectroscopy measurements

All measurements were performed at room temperature. We used a non-resonant linearly polarized Q-switched laser excitation at 532 nm wavelength with 5 ns pulse length (Opolette SE 355 LD). All photoluminescence measurements were acquired in a transmission geometry with a 50 mm focal length lens used for excitation. A spatial light modulator was used to shape the spatial profile of the pump beam into the array of Gaussian spots with full-width-at-half-maximum (FWHM) of $\approx 3 \mu\text{m}$ with the possibility of adding another pump spot provided by a parallel optical path with polarisation controlled independently by the $\lambda/2$ waveplate.

Output emission was collected using a 50x Mitutoyo microscope objective with a numerical aperture of 0.42 and coupled to a 550 mm spectrometer (Horiba Triax 550) equipped with a 300 grooves mm^{-1} grating and a mirror to provide spectral, wave-vector or spatial resolution depending on the set of lens used to focus the output on the entrance slit of the spectrometer and the width of the slit. All measurements above the threshold were carried out in a single-shot regime, while below the threshold we accumulated the signal for over 100 pulses.

The non-normalized Stokes parameters of the cavity emission are extracted using the following equation:

$$S_{1,2,3}(\mathbf{r}) = I_{H,D,\sigma^+}(\mathbf{r}) - I_{V,A,\sigma^-}(\mathbf{r}), \quad (3)$$

where $\mathbf{r} = (x, y)$ is the in-plane coordinate and $I_{H(V),D(A),\sigma^+(\sigma^-)}(\mathbf{r})$ corresponds to horizontally (vertically), diagonally (antidiagonally), and right-circularly(left-circularly) polarized (RCP and LCP for short) PL, respectively. The $S_1(\mathbf{r})$, $S_2(\mathbf{r})$, and $S_3(\mathbf{r})$ components represent the degree of linear, diagonal, and circular polarisations correspondingly. The total emission is written $S_0(\mathbf{r}) = I_{H,D,\sigma^+}(\mathbf{r}) + I_{V,A,\sigma^-}(\mathbf{r})$ and corresponding normalized Stokes parameters defined as $s_{1,2,3}(\mathbf{r}) = S_{1,2,3}(\mathbf{r})/S_0$.

4.3 Theoretical analysis: Non-Hermitian 2D Schrödinger Model (paraxial Maxwell-Bloch theory)

To describe the dynamics and coupling between spatially separated lasing states in the dye-filled LC microcavity [Fig. 1(a,b)], we propose a set of non-Hermitian 2D Schrödinger equations (NHSE) representing a paraxial limit of Maxwell-Bloch equations [47, 48] with additional terms based on rate equations describing a BODIPY-G1 dye-filled microcavity [43], which shares structural similarities with the P580 laser dye employed here. Under the slowly varying envelope approximation, we consider the photonic field within the LC microcavity in the linear polarization basis as $\psi = (\psi_{\parallel}, \psi_{\perp})^T$, where ψ_{\parallel} and ψ_{\perp} correspond to photons linearly polarized parallel and perpendicular to the nonresonant pump spots, respectively.

Without any loss of generality, we define the x and y directions in the cavity plane as our polarization basis and refer to them as the "horizontal" ψ_H and "vertical" ψ_V components. This choice yields the following system of equations:

$$i\hbar \frac{\partial \psi_{H,V}}{\partial t} = -\frac{\hbar^2}{2} \left\{ \left[\partial_x^2 \left(\frac{1}{m} \pm \frac{1}{\mu} \right) + \partial_y^2 \left(\frac{1}{m} \mp \frac{1}{\mu} \right) \right] + \hbar G(P_H + P_V) \right. \\ \left. + \frac{i\hbar}{2} (\gamma_{xp} n_{H,V} - \gamma_p) \right\} \psi_{H,V} \pm i \frac{\hbar^2}{\mu} \partial_x \partial_y \psi_{V,H} \pm \delta \psi_{H,V}. \quad (4)$$

Here, m denotes the effective photon mass within the microcavity, and μ represents the mass term accounting for the x - y polarization anisotropy induced by the transverse electric and magnetic (TE-TM) splitting of the birefringent LC medium [35]. This birefringence also causes an energy splitting δ between the horizontally and vertically polarized modes. Moreover, γ_{xp} is the decay rate describing the transfer of excitons from the non-resonantly pumped reservoir into the microcavity lasing mode, and γ_p characterizes the radiative losses from the lasing state to the outside of the microcavity.

The dynamics of the excitonic reservoir with density $n_{H,V}$ locally excited by a non-resonant Gaussian pump $P_{H,V} = p_{H,V} e^{-r^2/2w^2}$, with amplitude $p_{H,V}$ and width w , is accounted for by the following rate equation:

$$\frac{\partial n_{H,V}}{\partial t} = P_{H,V} - (2\gamma_{XX} + |\psi_{H,V}|^2 \gamma_{xp}) n_{H,V} + \gamma_{XX} n_{V,H}, \quad (5)$$

The parameter γ_{XX} describes the intermolecular energy transfer rate between n_H and n_V , characteristic of organic laser dyes [43]. The nonradiative relaxation of the excitonic reservoir γ_{NR} is safely neglected due to its smaller size compared to other decay rates within the model.

For the dyad lasing states under finite external voltage, the microcavity modes are within the Rashba-Dresselhaus SOC regime [35]. In this case, the polarization anisotropy is dominated by a term distinct from the TE-TM splitting as in Eq. (4),

and the dynamics of lasing states is described by the following equation:

$$i\hbar \frac{\partial \psi_{H,V}}{\partial t} = \left[-\frac{\hbar^2 \nabla^2}{2m} + \hbar G(P_H + P_V) \pm \delta + \frac{i\hbar}{2}(\gamma_{xp}n_{H,V} - \gamma_p) \right] \psi_{H,V} \pm i\delta_{\text{RD}}\partial_x \psi_{V,H}, \quad (6)$$

with $\nabla^2 \equiv \partial_x^2 + \partial_y^2$, and δ_{RD} being the strength of the Rashba-Dresselhaus splitting controlled by the applied external voltage.

In theoretical descriptions of typical inorganic semiconductor microcavities, corresponding NHSE commonly depict defocusing Kerr-like χ^3 nonlinear terms for characterizing energy blueshifts [58]. These explicit nonlinearities can be neglected here, as organic-filled microcavities are described in terms of highly localised Frenkel excitons, reducing pairwise interactions [43, 59]. However, other nonlinear sources responsible for pump-induced blueshifts are present in organic dye-filled microcavities, such as saturation of optical transitions [43]. In the case of LC microcavities, the blueshift can also result from the microcavity mode energy renormalization due to changes in the intracavity refractive index. To address these blueshift mechanisms, we introduce the phenomenological parameter G in Eqs. (4) and (6), whose value is set to fit the experimental measurements.

Based on the NHSE, we numerically obtain real-space and momentum space emission profiles for lasing states, considering both dyad and triad lasing modes (Secs. 2.2 and 2.4), as well as the case in which the coupling between the dyad lasing supermode is electrically tuned via external voltage (Sec. 2.3). All emission profiles were obtained considering external non-resonant pump amplitudes strong enough to ensure convergence to a finite-valued state $|\psi_{H,V}| \neq 0$ in the steady-state regime $\partial_t |\psi_{H,V}| = 0$. Initial conditions were chosen to be white-noise with random seed based on time of day.

For the case of dyad lasing supermodes shown in Fig. 2 corresponding to zero-voltage, we extracted the following parameters: microcavity photon effective masses $m = 0.0463 \text{ meV ps}^2 \mu\text{m}^{-2}$ and $\mu = 0.1835 \text{ meV ps}^2 \mu\text{m}^{-2}$, exciton reservoir to microcavity lasing mode decay rate $\gamma_p = 5.2632 \text{ ps}^{-1}$, lasing state radiative losses $\gamma_{xp} = 0.02 \mu\text{m}^2 \text{ ps}^{-1}$ and TE-TM energy splitting $\delta = 4.5 \text{ meV}$. We consider the intermolecular energy transfer ratio $\gamma_{XX} = 0.033 \text{ ps}^{-1}$ corresponding to a BODIPY-G1 dye-filled microcavity [43], which shares a similar structure with the P580 laser dye employed here. The results from our numerical simulation for both real- and momentum-space emission are shown in panels (j) and (k) of Fig. 2, respectively.

For the situation of electric control of coupling in the dyad configuration depicted in Fig. 4, we used the same parameters above for obtaining the corresponding simulations shown in Fig. 5, except for the effective mass $m = 0.048 \text{ meV ps}^2 \mu\text{m}^{-2}$, $\delta = 0$ and the strength of Rashba-Dresselhaus splitting $\delta_{\text{RD}} = 7 \text{ meV } \mu\text{m}$ for $V = 1840 \text{ mV}$. The same value of δ_{RD} is extracted for $V = 1880 \text{ mV}$, but with an additional horizontal-vertical linear polarization splitting at $\delta = 2.0 \text{ meV}$. In all simulations, we set the phenomenological parameter $G = 0.1 \mu\text{m}^2$ to mimic nonlinear energy blueshifts.

Supplementary information. Supplementary information provides additional details on voltage, and pump polarisation dependence of a single lasing state emission, interference measurements, and additional data on unconventional coupling. It also

provides additional numerical simulations of the NHSE, and estimation of light-matter coupling strength within our system.

Acknowledgements. The authors acknowledge the support of the European Union’s Horizon 2020 program through a FET Open research and innovation action under grant agreement no. 964770 (TopoLight). L.S.R. and H.S. acknowledge the Icelandic Research Fund (Rannís), grant No. 239552-051. H.S. acknowledges the project No. 2022/45/P/ST3/00467 co-funded by the Polish National Science Center and the European Union Framework Programme for Research and Innovation Horizon 2020 under the Marie Skłodowska-Curie grant agreement No. 945339. K.S. and S.D.L. acknowledge the Leverhulme Trust, grant No. RPG-2022-037.

Declarations

Author contributions

D.D. designed and implemented the experimental setup; D.D. and K.S. conducted the single-shot measurements; D.D. and P.Ko. analysed the experimental results; P.Ko., D.S., G.M. contributed with the results interpretation and data analysis, developed approach to determine the type of light-matter coupling regime; L.S.R. and H.S. performed theoretical modelling; P.N., P.M., W.P., P.Ku. designed and fabricated the liquid-crystal dye-filled microcavity and supervised sample fabrication within the project; M.M., P.Ka. characterised the sample after fabrication; D.D, L.S.R., H.S wrote the paper with input from all authors. J.S. and S.D.L. supervised the research.

Competing interests

The authors declare no competing interests.

References

- [1] Forbes, A., Oliveira, M., Dennis, M.R.: Structured light. *Nature Photonics* **15**(4), 253–262 (2021) <https://doi.org/10.1038/s41566-021-00780-4>
- [2] Piccardo, M., Oliveira, M., Toma, A., Aglieri, V., Forbes, A., Ambrosio, A.: Vortex laser arrays with topological charge control and self-healing of defects. *Nature Photonics* **16**(5), 359–365 (2022) <https://doi.org/10.1038/s41566-022-00986-0>
- [3] Parto, M., Hayenga, W., Marandi, A., Christodoulides, D.N., Khajavikhan, M.: Realizing spin Hamiltonians in nanoscale active photonic lattices. *Nature Materials* **19**(7), 725–731 (2020) <https://doi.org/10.1038/s41563-020-0635-6>
- [4] Berloff, N.G., Silva, M., Kalinin, K., Askitopoulos, A., Töpfer, J.D., Cilibrizzi, P., Langbein, W., Lagoudakis, P.G.: Realizing the classical xy hamiltonian in polariton simulators. *Nature Materials* **16**(11), 1120–1126 (2017) <https://doi.org/10.1038/nmat4971>

- [5] Chen, Z., Sludds, A., Davis, R., Christen, I., Bernstein, L., Ateshian, L., Heuser, T., Heermeier, N., Lott, J.A., Reitzenstein, S., Hamerly, R., Englund, D.: Deep learning with coherent VCSEL neural networks. *Nature Photonics* **17**(8), 723–730 (2023) <https://doi.org/10.1038/s41566-023-01233-w> arXiv:2207.05329
- [6] Matuszewski, M., Prystupiuk, A., Opala, A.: Role of all-optical neural networks. *Phys. Rev. Appl.* **21**, 014028 (2024) <https://doi.org/10.1103/PhysRevApplied.21.014028>
- [7] Tanaka, G., Yamane, T., Héroux, J.B., Nakane, R., Kanazawa, N., Takeda, S., Numata, H., Nakano, D., Hirose, A.: Recent advances in physical reservoir computing: A review. *Neural Networks* **115**, 100–123 (2019) <https://doi.org/10.1016/j.neunet.2019.03.005>
- [8] Ballarini, D., Gianfrate, A., Panico, R., Opala, A., Ghosh, S., Dominici, L., Ardizzone, V., De Giorgi, M., Lerario, G., Gigli, G., Liew, T.C.H., Matuszewski, M., Sanvitto, D.: Polaritonic neuromorphic computing outperforms linear classifiers. *Nano Letters* **20**(5), 3506–3512 (2020) <https://doi.org/10.1021/acs.nanolett.0c00435>
- [9] Ngcobo, S., Litvin, I., Burger, L., Forbes, A.: A digital laser for on-demand laser modes. *Nature Communications* **4**(1), 2289 (2013) <https://doi.org/10.1038/ncomms3289>
- [10] Kumar Reddy, A.N., Mahler, S., Goldring, A., Pal, V., Friesem, A.A., Davidson, N.: Phase locking of lasers with Gaussian coupling. *Optics Express* **30**(2), 1114 (2022) <https://doi.org/10.1364/OE.439957>
- [11] Ma, Y., Lan, T., Wang, X., Ruan, R., Cao, Y., Dai, J., Wang, Z.: Phase-locking dynamics of a 2D VCSEL hexagonal array with an integrated Talbot cavity. *Optics Express* **30**(6), 9892 (2022) <https://doi.org/10.1364/OE.452548>
- [12] Pan, G., Xun, M., Zhou, X., Sun, Y., Dong, Y., Wu, D.: Harnessing the capabilities of VCSELs: unlocking the potential for advanced integrated photonic devices and systems. *Light: Science & Applications* **13**(1), 229 (2024) <https://doi.org/10.1038/s41377-024-01561-8>
- [13] Xie, Y.-Y., Ni, P.-N., Wang, Q.-H., Kan, Q., Briere, G., Chen, P.-P., Zhao, Z.-Z., Delga, A., Ren, H.-R., Chen, H.-D., Xu, C., Genevet, P.: Metasurface-integrated vertical cavity surface-emitting lasers for programmable directional lasing emissions. *Nature Nanotechnology* **15**(2), 125–130 (2020) <https://doi.org/10.1038/s41565-019-0611-y>
- [14] Miyai, E., Sakai, K., Okano, T., Kunishi, W., Ohnishi, D., Noda, S.: Lasers producing tailored beams. *Nature* **441**(7096), 946–946 (2006) <https://doi.org/10.1038/441946a>

- [15] Raftery, J.J., Danner, A.J., Lee, J.C., Choquette, K.D.: Coherent coupling of two-dimensional arrays of defect cavities in photonic crystal vertical cavity surface-emitting lasers. *Applied Physics Letters* **86**(20), 1–3 (2005) <https://doi.org/10.1063/1.1929074>
- [16] Noda, S., Yoshida, M., Inoue, T., De Zoysa, M., Ishizaki, K., Sakata, R.: Photonic-crystal surface-emitting lasers. *Nature Reviews Electrical Engineering* **1**(12), 802–814 (2024) <https://doi.org/10.1038/s44287-024-00113-x>
- [17] Kasprzak, J., Richard, M., Kundermann, S., Baas, A., Jeambrun, P., Keeling, J.M.J., Marchetti, F., Szymańska, M., André, R., Staehli, J.a., *et al.*: Bose–einstein condensation of exciton polaritons. *Nature* **443**(7110), 409–414 (2006)
- [18] Töpfer, J.D., Chatzopoulos, I., Sigurdsson, H., Cookson, T., Rubo, Y.G., Lagoudakis, P.G.: Engineering spatial coherence in lattices of polariton condensates. *Optica* **8**(1), 106 (2021) <https://doi.org/10.1364/optica.409976>
- [19] Alyatkin, S., Töpfer, J.D., Askitopoulos, A., Sigurdsson, H., Lagoudakis, P.G.: Optical Control of Couplings in Polariton Condensate Lattices. *Physical Review Letters* **124**(20), 207402 (2020) <https://doi.org/10.1103/PhysRevLett.124.207402>
- [20] Kavokin, A., Liew, T.C.H., Schneider, C., Lagoudakis, P.G., Klembt, S., Hoefling, S.: Polariton condensates for classical and quantum computing. *Nature Reviews Physics* **4**(7), 435–451 (2022) <https://doi.org/10.1038/s42254-022-00447-1>
- [21] Opala, A., Matuszewski, M.: Harnessing exciton-polaritons for digital computing, neuromorphic computing, and optimization [invited]. *Opt. Mater. Express* **13**(9), 2674–2689 (2023) <https://doi.org/10.1364/OME.496985>
- [22] Tao, R., Peng, K., Haeberlé, L., Li, Q., Jin, D., Fleming, G.R., Kéna-Cohen, S., Zhang, X., Bao, W.: Halide perovskites enable polaritonic XY spin Hamiltonian at room temperature. *Nature Materials* **21**(7), 761–766 (2022) <https://doi.org/10.1038/s41563-022-01276-4>
- [23] Cookson, T., Kalinin, K., Sigurdsson, H., Töpfer, J.D., Alyatkin, S., Silva, M., Langbein, W., Berloff, N.G., Lagoudakis, P.G.: Geometric frustration in polygons of polariton condensates creating vortices of varying topological charge. *Nature Communications* **12**(1), 2120 (2021) <https://doi.org/10.1038/s41467-021-22121-3>
- [24] Werner, Z., Frączak, A., Daniélsson, V.K., Szczytko, J., Piętka, B., Sigurdsson, H.: Discrete chiral ballistic polariton laser. *Laser & Photonics Reviews* (2025) <https://doi.org/10.1002/lpor.202500195>
- [25] Pickup, L., Sigurdsson, H., Ruostekoski, J., Lagoudakis, P.G.: Synthetic

- band-structure engineering in polariton crystals with non-hermitian topological phases. *Nature Communications* **11**(1) (2020) <https://doi.org/10.1038/s41467-020-18213-1>
- [26] Pieczarka, M., Estrecho, E., Ghosh, S., Wurdack, M., Steger, M., Snoke, D.W., West, K., Pfeiffer, L.N., Liew, T.C.H., Truscott, A.G., Ostrovskaya, E.A.: Topological phase transition in an all-optical exciton-polariton lattice. *Optica* **8**(8), 1084 (2021) <https://doi.org/10.1364/optica.426996> arXiv:2102.01262
- [27] Betzold, S., Dürerth, J., Dusel, M., Emmerling, M., Bieganowska, A., Ohmer, J., Fischer, U., Höfling, S., Klembt, S.: Dirac cones and room temperature polariton lasing evidenced in an organic honeycomb lattice. *Advanced Science* **11**(21) (2024) <https://doi.org/10.1002/advs.202400672>
- [28] Sanvitto, D., Kéna-Cohen, S.: The road towards polaritonic devices. *Nature Materials* **15**(10), 1061–1073 (2016) <https://doi.org/10.1038/nmat4668>
- [29] Ghosh, S., Su, R., Zhao, J., Fieramosca, A., Wu, J., Li, T., Zhang, Q., Li, F., Chen, Z., Liew, T., Sanvitto, D., Xiong, Q.: Microcavity exciton polaritons at room temperature. *Photonics Insights* **1**(1), 04 (2022) <https://doi.org/10.3788/pi.2022.r04>
- [30] Zasedatelev, A.V., Baranikov, A.V., Sannikov, D., Urbonas, D., Scafrimuto, F., Shishkov, V.Y., Andrianov, E.S., Lozovik, Y.E., Scherf, U., Stöferle, T., Mahrt, R.F., Lagoudakis, P.G.: Single-photon nonlinearity at room temperature. *Nature* **597**(7877), 493–497 (2021) <https://doi.org/10.1038/s41586-021-03866-9>
- [31] Plumhof, J.D., Stöferle, T., Mai, L., Scherf, U., Mahrt, R.F.: Room-temperature Bose–Einstein condensation of cavity exciton–polaritons in a polymer. *Nature Materials* **13**(3), 247–252 (2014) <https://doi.org/10.1038/nmat3825>
- [32] Zasedatelev, A.V., Baranikov, A.V., Urbonas, D., Scafrimuto, F., Scherf, U., Stöferle, T., Mahrt, R.F., Lagoudakis, P.G.: A room-temperature organic polariton transistor. *Nature Photonics* **13**(6), 378–383 (2019) <https://doi.org/10.1038/s41566-019-0392-8>
- [33] Dusel, M., Betzold, S., Egorov, O.A., Klembt, S., Ohmer, J., Fischer, U., Höfling, S., Schneider, C.: Room temperature organic exciton–polariton condensate in a lattice. *Nature Communications* **11**(1), 2863 (2020) <https://doi.org/10.1038/s41467-020-16656-0> arXiv:1907.05065
- [34] McGhee, K.E., Jayaprakash, R., Georgiou, K., Burg, S.L., Lidzey, D.G.: Polariton condensation in a microcavity using a highly-stable molecular dye. *Journal of Materials Chemistry C* **10**(11), 4187–4195 (2022) <https://doi.org/10.1039/D1TC05554B>

- [35] Rechcińska, K., Król, M., Mazur, R., Morawiak, P., Mirek, R., Łempicka, K., Bardyszewski, W., Matuszewski, M., Kula, P., Piecek, W., Lagoudakis, P.G., Piętka, B., Szczytko, J.: Engineering spin-orbit synthetic Hamiltonians in liquid-crystal optical cavities. *Science* **366**(6466), 727–730 (2019) <https://doi.org/10.1126/science.aay4182> <https://www.science.org/doi/pdf/10.1126/science.aay4182>
- [36] Łempicka-Mirek, K., Król, M., De Marco, L., Coriolano, A., Polimeno, L., Viola, I., Kędziora, M., Muszyński, M., Morawiak, P., Mazur, R., Kula, P., Piecek, W., Fita, P., Sanvitto, D., Szczytko, J., Piętka, B.: Electrical polarization switching of perovskite polariton laser. *Nanophotonics* **13**(14), 2659–2668 (2024) <https://doi.org/10.1515/nanoph-2023-0829>
- [37] Lekenta, K., Król, M., Mirek, R., Łempicka, K., Stephan, D., Mazur, R., Morawiak, P., Kula, P., Piecek, W., Lagoudakis, P.G., Piętka, B., Szczytko, J.: Tunable optical spin Hall effect in a liquid crystal microcavity. *Light: Science & Applications* **7**(1), 74 (2018) <https://doi.org/10.1038/s41377-018-0076-z>
- [38] Liang, J., Wen, W., Jin, F., Rubo, Y.G., Liew, T.C.H., Su, R.: Polariton spin hall effect in a rashba–dresselhaus regime at room temperature. *Nature Photonics* **18**(4), 357–362 (2024) <https://doi.org/10.1038/s41566-023-01375-x>
- [39] Król, M., Rechcińska, K., Sigurdsson, H., Oliwa, P., Mazur, R., Morawiak, P., Piecek, W., Kula, P., Lagoudakis, P.G., Matuszewski, M., Bardyszewski, W., Piętka, B., Szczytko, J.: Realizing Optical Persistent Spin Helix and Stern-Gerlach Deflection in an Anisotropic Liquid Crystal Microcavity. *Physical Review Letters* **127**(19), 190401 (2021) <https://doi.org/10.1103/PhysRevLett.127.190401>
- [40] Łempicka-Mirek, K., Król, M., Sigurdsson, H., Wincukiewicz, A., Morawiak, P., Mazur, R., Muszyński, M., Piecek, W., Kula, P., Stefaniuk, T., Kamińska, M., De Marco, L., Lagoudakis, P.G., Ballarini, D., Sanvitto, D., Szczytko, J., Piętka, B.: Electrically tunable Berry curvature and strong light-matter coupling in liquid crystal microcavities with 2D perovskite. *Science Advances* **8**(40), 1–11 (2022) <https://doi.org/10.1126/sciadv.abq7533> [arXiv:2203.05289](https://arxiv.org/abs/2203.05289)
- [41] Muszyński, M., Król, M., Rechcińska, K., Oliwa, P., Kędziora, M., Łempicka-Mirek, K., Mazur, R., Morawiak, P., Piecek, W., Kula, P., Lagoudakis, P.G., Piętka, B., Szczytko, J.: Realizing Persistent-Spin-Helix Lasing in the Regime of Rashba-Dresselhaus Spin-Orbit Coupling in a Dye-Filled Liquid-Crystal Optical Microcavity. *Physical Review Applied* **17**(1), 014041 (2022) <https://doi.org/10.1103/PhysRevApplied.17.014041>
- [42] Weihs, G., Deng, H., Snoke, D., Yamamoto, Y.: Polariton lasing vs. photon lasing in a semiconductor microcavity. *physica status solidi (a)* **201**(4), 625–632 (2004) <https://doi.org/10.1002/pssa.200304061>

- [43] Yagafarov, T., Sannikov, D., Zasedatelev, A., Georgiou, K., Baranikov, A., Kyriienko, O., Shelykh, I., Gai, L., Shen, Z., Lidzey, D., Lagoudakis, P.: Mechanisms of blueshifts in organic polariton condensates. *Communications Physics* **3**(1), 18 (2020) <https://doi.org/10.1038/s42005-019-0278-6>
- [44] Putintsev, A.D., McGhee, K.E., Sannikov, D., Zasedatelev, A.V., Töpfer, J.D., Jessewitsch, T., Scherf, U., Lidzey, D.G., Lagoudakis, P.G.: Controlling the Spatial Profile and Energy Landscape of Organic Polariton Condensates in Double-Dye Cavities. *Physical Review Letters* **131**(18), 186902 (2023) <https://doi.org/10.1103/PhysRevLett.131.186902>
- [45] Langbein, W., Hvam, J.M.: Elastic Scattering Dynamics of Cavity Polaritons: Evidence for Time-Energy Uncertainty and Polariton Localization. *Physical Review Letters* **88**(4), 047401 (2002) <https://doi.org/10.1103/PhysRevLett.88.047401>
- [46] Töpfer, J.D., Sigurdsson, H., Pickup, L., Lagoudakis, P.G.: Time-delay polaritonics. *Communications Physics* **3**(1) (2020) <https://doi.org/10.1038/s42005-019-0271-0>
- [47] Ning, C.-Z., Indik, R., Moloney, J.: Effective Bloch equations for semiconductor lasers and amplifiers. *IEEE Journal of Quantum Electronics* **33**(9), 1543–1550 (1997)
- [48] Berloff, N., Keeling, J.: Universality in modelling non-equilibrium pattern formation in polariton condensates. In: *Physics of Quantum Fluids: New Trends and Hot Topics in Atomic and Polariton Condensates*, pp. 19–38. Springer, Berlin, Heidelberg (2013)
- [49] Pal, V., Mahler, S., Tradonsky, C., Friesem, A.A., Davidson, N.: Rapid fair sampling of the XY spin Hamiltonian with a laser simulator. *Physical Review Research* **2**(3), 1–8 (2020) <https://doi.org/10.1103/PhysRevResearch.2.033008> [arXiv:1912.10689](https://arxiv.org/abs/1912.10689)
- [50] Kalinin, K.P., Berloff, N.G.: Computational complexity continuum within Ising formulation of NP problems. *Communications Physics* **5**(1), 20 (2022) <https://doi.org/10.1038/s42005-021-00792-0>
- [51] Dovzhenko, D., Aristov, D., Pickup, L., Sigurdsson, H., Lagoudakis, P.: Next-nearest-neighbor coupling with spinor polariton condensates. *Physical Review B* **108**(16), 161301 (2023) <https://doi.org/10.1103/PhysRevB.108.L161301> [arXiv:2301.04210](https://arxiv.org/abs/2301.04210)
- [52] Tseses, S., Ostrovsky, E., Cohen, K., Gjonaj, B., Lindner, N.H., Bartal, G.: Optical skyrmion lattice in evanescent electromagnetic fields. *Science* **361**(6406), 993–996 (2018) <https://doi.org/10.1126/science.aau0227>

- [53] Yang, L., Li, G., Gao, X., Lu, L.: Topological-cavity surface-emitting laser. *Nature Photonics* **16**(4), 279–283 (2022) <https://doi.org/10.1038/s41566-022-00972-6>
- [54] Mahler, S., Bernstein, E., Gadasi, S., Arwas, G., Friesem, A.A., Davidson, N.: Programmable all optical spin simulator with artificial gauge fields, 1–6 (2024) [arXiv:2408.13865](https://arxiv.org/abs/2408.13865)
- [55] Zuo, Y., Li, B., Zhao, Y., Jiang, Y., Chen, Y.-C., Chen, P., Jo, G.-B., Liu, J., Du, S.: All-optical neural network with nonlinear activation functions. *Optica* **6**(9), 1132 (2019) <https://doi.org/10.1364/OPTICA.6.001132> [arXiv:1904.10819](https://arxiv.org/abs/1904.10819)
- [56] Dąbrowski, R., Kula, P., Herman, J.: High Birefringence Liquid Crystals. *Crystals* **3**(3), 443–482 (2013) <https://doi.org/10.3390/cryst3030443>
- [57] Miszczyk, E., Mazur, R., Morawiak, P., Mrukiewicz, M., Piecek, W., Raszewski, Z., Kula, P., Kowiorski, K., Kędzierski, J., Zieliński, J.: Refractive index matched liquid crystal cell for laser metrology application. *Liquid Crystals* **45**(11), 1690–1698 (2018) <https://doi.org/10.1080/02678292.2018.1471745>
- [58] Wouters, M., Carusotto, I.: Excitations in a nonequilibrium Bose-Einstein condensate of exciton polaritons. *Phys. Rev. Lett.* **99**, 140402 (2007) <https://doi.org/10.1103/PhysRevLett.99.140402>
- [59] Daskalakis, K.S., Maier, S.A., Murray, R., Kéna-Cohen, S.: Nonlinear interactions in an organic polariton condensate. *Nature Materials* **13**(3), 271–278 (2014) <https://doi.org/10.1038/nmat3874>

Supplemental information: Electrically Reconfigurable Extended Lasing State in an Organic Liquid-Crystal Microcavity

Dmitriy Dovzhenko^{1*}, Luciano Siliano Ricco², Krzysztof Sawicki¹,
Marcin Muszyński³, Pavel Kokhanchik⁴, Piotr Kapuściński³,
Przemysław Morawiak⁵, Wiktor Piecek⁵, Piotr Nyga⁶,
Przemysław Kula⁵, Dmitry Solnyshkov^{4,8}, Guillaume Malpuech⁴,
Helgi Sigurðsson^{2,3}, Jacek Szczytko³, Simone De Liberato^{1,9}

¹School of Physics and Astronomy, University of Southampton,
University Road, Southampton, SO17 1BJ, United Kingdom.

²Science Institute, University of Iceland, Dunhagi-3, Reykjavik, IS-107,
Iceland.

³Institute of Experimental Physics, Faculty of Physics, University of
Warsaw, ulica Pasteura 5, Warsaw, PL-02-093, Poland.

⁴Institut Pascal, Université Clermont Auvergne, CNRS, ClermontINP,
Clermont-Ferrand, F-63000, France.

⁵Institute of Applied Physics, Military University of Technology, S.
Kaliskiego 2, Warsaw, 00-908, Poland.

⁶Institute of Optoelectronics, Military University of Technology, S.
Kaliskiego 2, Warsaw, 00-908, Poland.

⁷Institute of Chemistry, Military University of Technology, S. Kaliskiego
2, Warsaw, 00-908, Poland.

⁸Institut Universitaire de France, Paris, F-75231, France.

⁹Istituto di Fotonica e Nanotecnologie, Consiglio Nazionale delle
Ricerche (CNR), Piazza Leonardo da Vinci 32, Milano, 20133, Italy.

*Corresponding author(s). E-mail(s): dovzhenkods@gmail.com;

1 Details on the sample properties and experimental results

1.1 Individual lasing state emission properties

We note that below the threshold, despite the vertical polarisation of the excitation, we observed emission from both horizontal and vertical cavity modes due to the ultra-fast intermolecular energy transfer mechanism responsible for the depolarisation of the photoluminescence (PL) in films of organic laser dyes with similar structure and properties [1, 2]. In contrast when pump power exceeds the threshold we observed sharp increase of the degree of linear polarisation with the polarisation of the lasing state inherited from the polarisation of the pump, see Fig. 1.

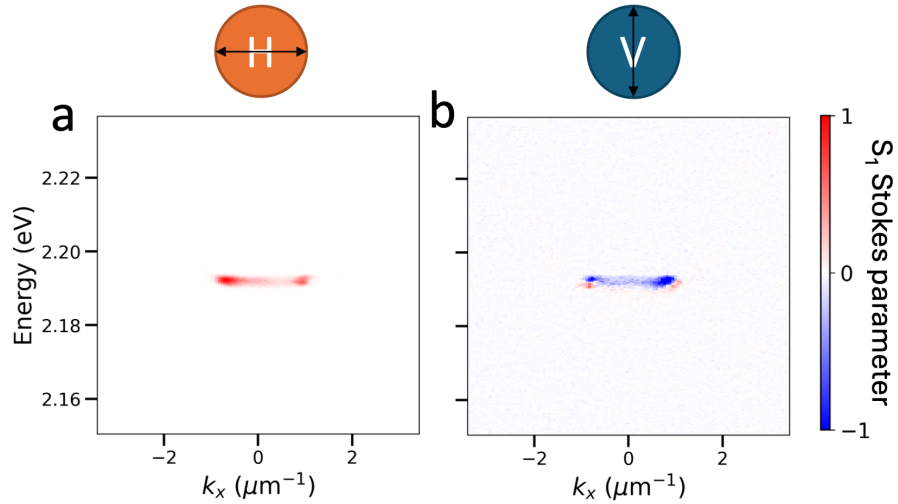


Fig. 1 Inheritance of the lasing state polarisation. (a,b) Energy-resolved along $k_y = 0$ momentum-space distribution of the non-normalised S_1 Stokes component of the emission from a single spot pumped with (a) horizontally and (b) vertically polarised light. Schematic above shows the respective polarisation of the pump

Fig. 2 shows characteristics of the PL for a single isolated lasing state around Rashba-Dresselhaus (RD) regime of spin-orbit coupling (SOC). In Fig. 2(a,b) we show energy-resolved momentum space PL below the lasing threshold measured (a) exactly in RD SOC regime at 1840 mV and (b) in slightly detuned regime at 1880 mV external voltage. We further demonstrate the polarisation properties the emission in each regime providing momentum-space distribution of the non-normalised S_3 (Fig. 2(c)) and S_1 (Fig. 2(d)) Stokes components of the lasing state.

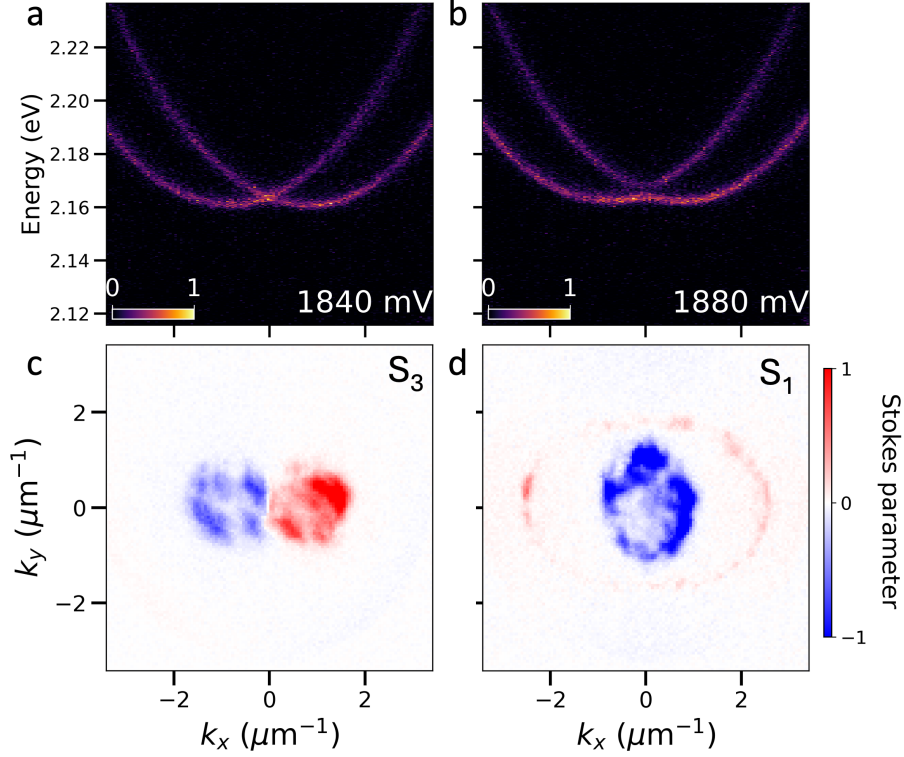


Fig. 2 Emission characteristics of a single lasing state. (a,b) Energy-resolved momentum-space along $k_y = 0$ for two values of external voltage, corresponding to (a) 1840 mV and (b) 1880 mV pumped below ($0.5P_{th}$) the lasing threshold and (c,d) corresponding momentum-space distribution of the non-normalised S_3 (c) and S_1 (d) Stokes components of the lasing state pumped above ($1.5P_{th}$) the lasing threshold.

1.2 Spatial coherence in a dyad supermode

To further support the claim of phase-locking between the spatially separated lasing states and electrical tunability of such effect we performed spatially resolved interferometry measurements for the case of dyad supermode with the spot separation distance of $13 \mu\text{m}$, Fig. 3. Single shot interferometry measurements were made using Mach-Zehnder interferometer at 0 time delay to spatially overlap the real space emission from the opposite lasing states of a dyad (see schematic in Fig. 3). We observed clear interference fringes for 0 V (Fig. 3(a)), highlighting the synchronization between the states. Increase of the voltage to 1.6 V was accompanied by the loss of fringes visibility corresponding to desynchronization, while further increase to 1.84 V showed revival of the fringes visibility and re-establishing of the phase-locking in a dyad. We

therefore prove that the appearance of the fringe pattern in the real- and momentum-space of the emission from the array of spatially extended lasing states is accompanied by a long-range phase-coherence.

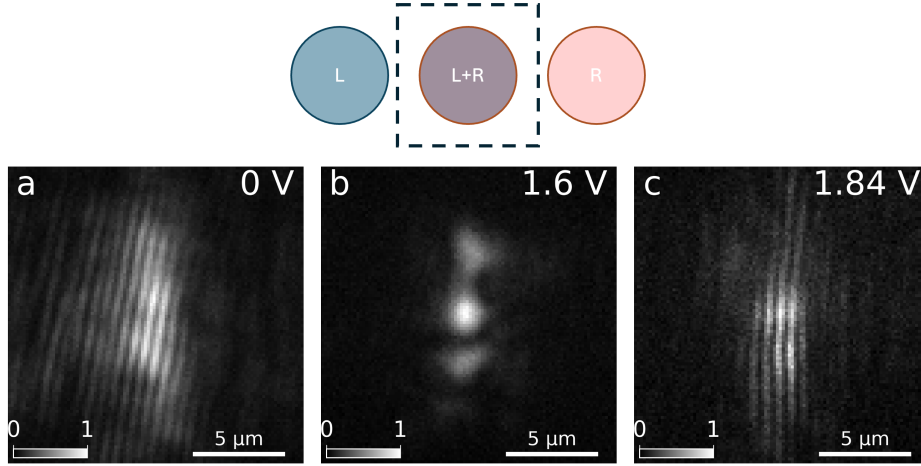


Fig. 3 Spatially extended coherence. Experimental interferogram of the dyad supermode obtained by overlapping the real-space emission of the opposite lasing states of a dyad going through the separate arms of Mach-Zehnder interferometer at **(a)** 0 V, **(b)** 1.6 V, **(c)** 1.84 V. Schematic above represents the overlapping real-space emission of a dyad (left and right circles) from the different (red and blue) arms of the interferometer with the region depicted in images below shown by dashed square.

1.3 Additional data on unconventional coupling

In Sec. 2.4 of the manuscript we demonstrate realisation of next-nearest-neighbour (NNN) coupling regime by analysing the periodicity of interference fringes visible in momentum space. In Fig. 4 we show polarisation resolved PL in momentum space for NNN regime of interaction corresponding to Fig.6(f) of the main manuscript. Phase-locking is manifested between horizontally polarised states, while no interference fringes are observed in vertically polarised emission.

2 Determination of the coupling by extracting photonic component

The standard way of strong coupling determination is the observation of cavity mode anticrossing while the photonic mode approaches the exciton $||$. In our sample any photonic mode has a parabolic shape and does not demonstrate anticrossing. More precisely, any mode vanishes before we start seeing anticrossing both at the high wavevector or at the low wavevector when it is shifted towards the exciton, which is

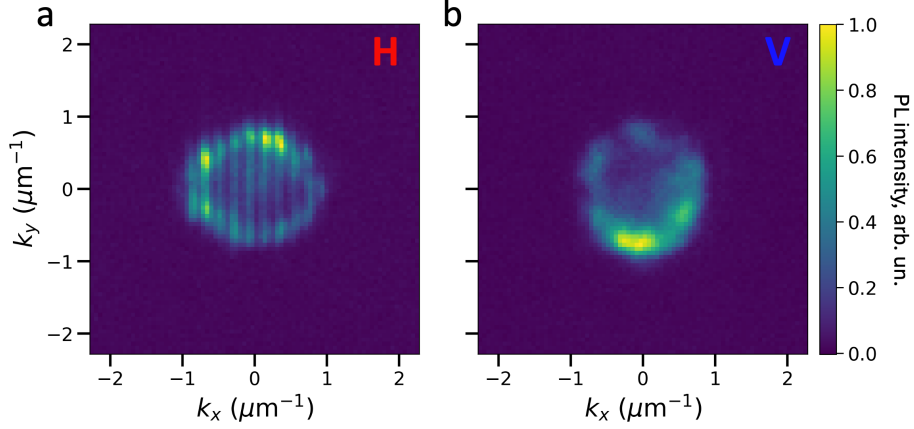


Fig. 4 Emission characteristics of a single lasing state. Horizontally (a) and vertically (b) polarised momentum-space distribution of the emission from 3 lasing states in the NNN coupling regime.

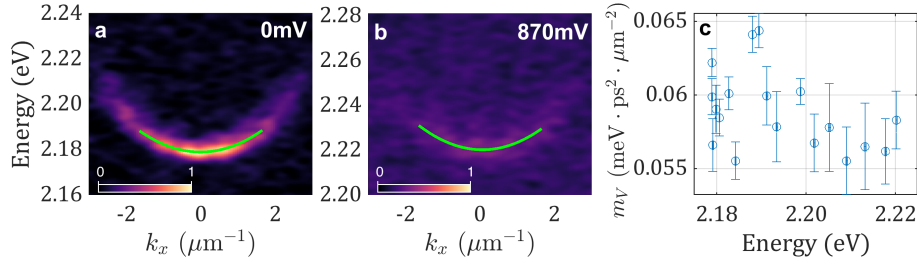


Fig. 5 Experimental dispersion of the tunable vertically-polarized cavity mode below the lasing threshold for the voltage of (a) 0 mV and (b) 870 mV; the green line demonstrates the fitting by a parabola; (c) extracted mode mass for different voltages by fitting with a parabolic function; error bars include only a fitting error and do not include experimental uncertainties; the mode mass does not increase while approaching the excitonic resonance, therefore, the mode is in the weak coupling regime.

applicable for tunable vertically polarized modes. However, as it has been shown in a recent study [3], when the exciton resonance is widely inhomogeneously broadened, the absence of anticrossing does not signify the absence of strong coupling for high exciton-photon detunings. A more detailed analysis of modes is needed which we perform in the following.

We follow a tunable vertically polarized photonic mode for different values of applied voltage until it vanishes due to the proximity to the exciton located at 2.4 eV for the dye P580. For each value of voltage, we fit the mode with a parabola, as shown in Fig. 5(a,b) for two values of voltage (all dispersions for voltage values

in-between demonstrate a good fit by parabola as well with coefficient of determination $R^2 > 0.96$). We extract the effective mass and the bottom (mode) energy of each parabola and plot them together in Fig. 5(c). In the case of the strong coupling, this dependence has to show a gradual increase of the mode mass when approaching the exciton [3]. In our case, we see that the mass remains approximately constant. Therefore, we conclude that the sample is in the weak coupling regime.

3 Simulations with Generalized Gross-Pitaevskii Model

This section presents additional data for simulated real and Fourier-space distributions using the Gross-Pitaevskii model as described in section 4.3 of the main text. Particularly, in Fig. 6 we show the simulations for the dyad supermode lasing states as a function of the distance between pump spots, corresponding to cases depicted in Fig. 2 of the main text. We also depict numerical simulations for the case of unconventional coupling in 1D chain of pump spots as seen in Fig. 7, corresponding to experimental profiles from Fig. 5 in the main text.

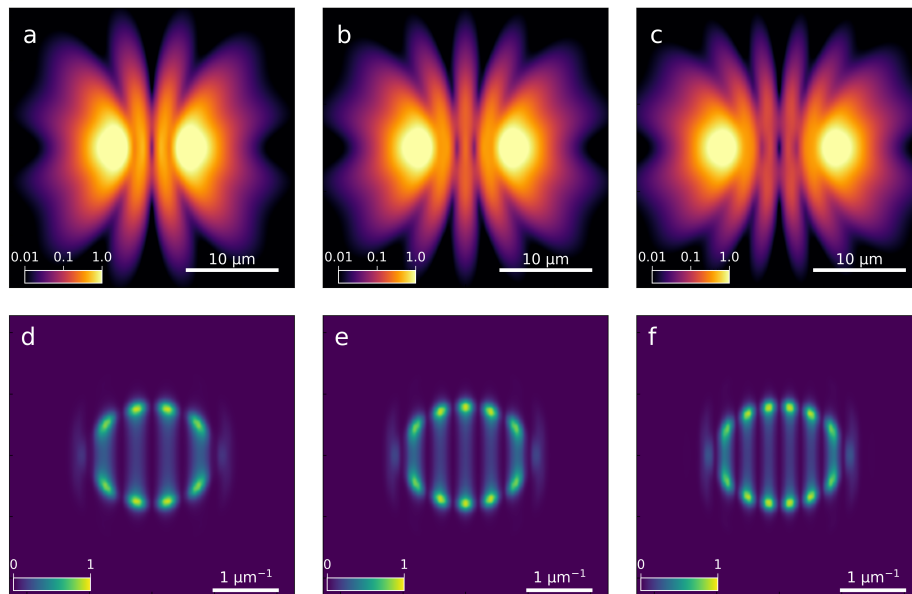


Fig. 6 Simulation for the dyad supermode lasing state for distinct distances d between pump spots, corresponding to profiles shown in Fig. 2 of the main text. Panels (a,d) exhibit real and Fourier-space profiles for $d = 9\mu\text{m}$, while (b,e) and (d,f) correspond to $d = 11\mu\text{m}$ and $d = 13\mu\text{m}$, respectively.

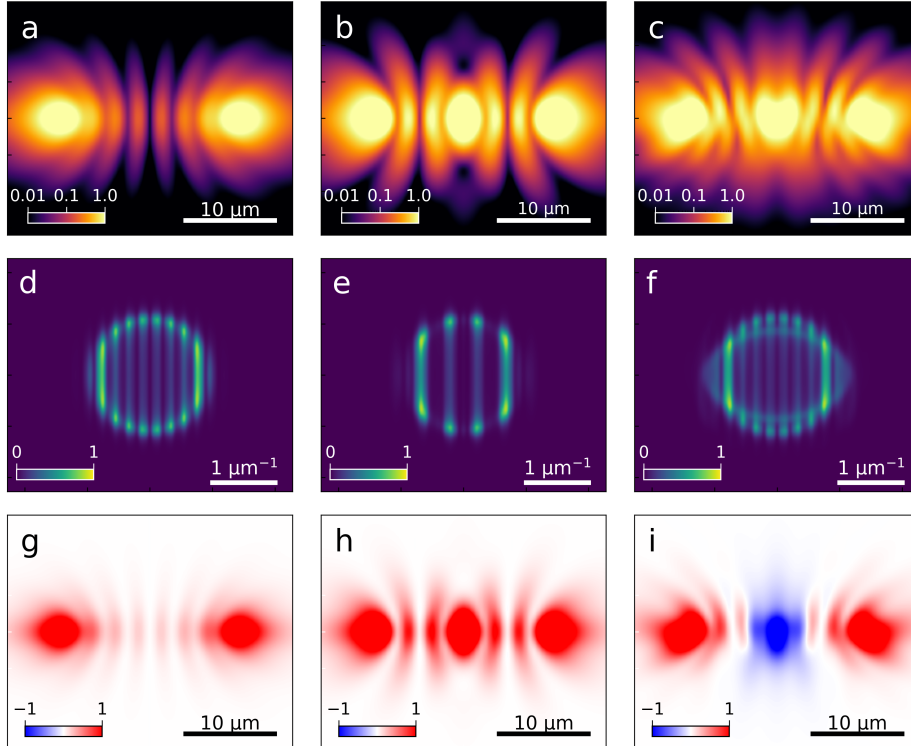


Fig. 7 Simulation for an unconventional coupling in a 1D chain of pump spots corresponding to emission profiles shown in Fig. 5 of the main text. The top and middle panels show the numerical simulations for both real and Fourier-space profiles, with bottom panels exhibiting the real-space $S_1(\mathbf{r})$ component of the Stokes vector describing the degree of linear polarisation emission profile as defined in Eq. (1) of the main text. (a,d,g) describes two vertically polarised pump spots at $20\mu\text{m}$ separation distance. (b,e,h) show the simulations for three vertically polarised pump spots separated by $10\mu\text{m}$ from each other. (c,f,i) also numerically describes three pump spots separated by $10\mu\text{m}$, but with the central spot pumped with horizontally polarised light.

References

- [1] Chang, M.H., Frampton, M.J., Anderson, H.L., Herz, L.M.: Intermolecular Interaction Effects on the Ultrafast Depolarization of the Optical Emission from Conjugated Polymers. *Physical Review Letters* **98**(2), 027402 (2007) <https://doi.org/10.1103/PhysRevLett.98.027402>
- [2] Musser, A.J., Rajendran, S.K., Georgiou, K., Gai, L., Grant, R.T., Shen, Z., Cavazzini, M., Ruseckas, A., Turnbull, G.A., Samuel, I.D.W., Clark, J., Lidzey, D.G.: Intermolecular states in organic dye dispersions: excimers vs. aggregates. *Journal of Materials Chemistry C* **5**(33), 8380–8389 (2017) <https://doi.org/10.1039/C7TC02655B>

- [3] Muszynski, M., Kokhanchik, P., Urbonas, D., Kapuscinski, P., Oliwa, P., Mirek, R., Georgakilas, I., Stoferle, T., Mahrt, R.F., Forster, M., et al.: Observation of a stripe phase in a spin-orbit coupled exciton-polariton bose-einstein condensate. arXiv preprint arXiv:2407.02406 (2024)